Top Catal (2016) 59:366–377
DOI 10.1007/s11244-015-0445-2

ORIGINAL PAPER

Metal Support Interaction Effects on the Reducibility of Ir Nanoparticles on Titania Nanotubes

José A. Toledo-Antonio[1] · Carlos Angeles-Chávez[1] · Ma. Antonia Cortés-Jácome[1] · I. Cuauhtémoc-López[1] · E. López-Salinas[1] · Ma. Lourdes Mosqueira[1] · G. Ferrat[1]

Published online: 18 August 2015

Abstract H_2IrCl_6 was impregnated on three types of materials: (i) anatase TiO_2 nanoparticles, (ii) anatase TiO_2 nanotubes and as a comparison, (iii) alumina Al_2O_3, with a view to reveal the effect of the support on Ir nanoparticles size, dispersion, morphologies, metal support interaction (MSI), and eventually on the catalytic activity in the hydrogenation of cyclohexene (CHE) at 273–303 K. Particularly, we focused on TiO_2 nanotubes as being scarcely examined as supports of Ir particles. Highly dispersed 1.3 nm half truncated cuboctahedral particles and full 1.4 nm cuboctahedral Ir nanoparticles on TiO_2 nanoparticles and TiO_2 nanotubes, respectively, were revealed by transmission electron microscopy and molecular modeling. These two, morphologically different TiO_2 supports show different MSI to Ir nanoparticles, affecting their metallic character and catalytic performance during CHE hydrogenation. At 273 K, complete cuboctahedral Ir particles (on TiO_2 nanotubes) showed a TOF of 4.7 s^{-1} which was slightly more active than truncated ones (on TiO_2 nanoparticles and Al_2O_3) showing a TOF of 3.2–3.7 s^{-1}. Iridium truncated nanoparticles were probably not completely reduced to Ir^0 and exhibited poor metallic character due to an electronic screening at the metal support interaction, which explain the different TOF in CHE hydrogenation.

✉ José A. Toledo-Antonio
jtoledo@imp.mx

[1] Instituto Mexicano del Petróleo, Eje Central Lázaro Cárdenas # 152, 07730 Mexico, DF, Mexico

Keywords Iridium nanoparticles · TiO_2 nanotube · Anatase · Cyclohexene hydrogenation/dehydrogenation · Metal support interaction

1 Introduction

Structural and morphological modification of materials made up of similar elemental components can induce changes on their optical, magnetic and electronic properties as well as in their chemical reactivity, inducing surprising and unexpected applications [1]. In catalysis for example, it is expected that new materials from nanotechnology catalyze chemical reactions at higher conversion and selectivity towards a desired product, with better energy efficiency and economical advantages, in comparison with present conventional catalysts. A clear example of these nanomaterials corresponds to supported noble metals, where the particle size is a crucial parameter, influencing the activity, selectivity and lifetime of catalysts [2, 3]. In metal nanoparticles of around 1 nm (e.g. tens of atoms), more than 90 % of atoms are located on the particle's exposed surface [4], and in addition, the atomic coordination number of $\sim$1 nm particles is smaller than that in larger nanoparticles (e.g. 12 in a fcc lattice), which have a substantial fraction of the atoms in the bulk inducing distinctly different catalytic performance [5].

The catalytic activity of the supported noble metal nanoparticles depends strongly on the nature of the support. Noble metals loaded on inert non-reducible supports, such as Al_2O_3 or SiO_2, produce good catalysts for structure-sensitive reactions (e.g. hydrogenolysis), and their reactivity is affected strongly by the metal dispersion [6]. On the other hand, metal nanoparticles deposited on a reducible support, such as TiO_2, result in catalysts for structure-

insensitive reactions (e.g. dehydrogenation), suppressing the hydrogenolysis reactions [7]. Such a remarkable difference in reactivity originates on a phenomenon named strong metal support interaction (SMSI), occurring on reducible supports. SMSI is due to the electronic interaction between metal nanoparticles and the semiconducting support, i.e. during reduction at temperatures higher than 573 K, an electron is transferred from the support's cation such, as Ti^{3+}, to the metal particle, inducing profound changes in catalytic activity, chemisorption properties and morphology of the metal particles [7, 8]. Particularly, in Ir/TiO_2 catalysts, SMSI suppresses the hydrogenolysis side reaction, favoring the dehydrogenation, and aromatization reactions that yield desired products, improving the selectivity of reforming catalysts, in comparison with that on Ir/Al_2O_3 support [9]. In contrast, on ring opening reaction of naphthenic molecules (C6-rings), Ir catalysts can operate under different mechanisms, depending strongly on the type of support used and only slightly on the metal dispersion [10]. Ir/TiO_2 causes mainly the C–C scission at a substituted position (e.g. olefin intermediates), which is crucial for improving diesel cetane number, whereas Ir/SiO_2 favors C–C rupture at an unsubstituted position (e.g. dicarbene reaction pathway) resulting in products with high degree of branching, which is also important, but for improving gasoline octane number [10].

The low specific surface area of a conventional titania anatase support is one of its greatest disadvantages. To overcome this limitation, titanium oxide, as in anatase phase, can been converted into titania nanotubes or nanofibers through a relatively simple alkaline hydrothermal method [11, 12]. This transformation yields materials with specific surface area as large as 400 $m^2\ g^{-1}$ [11, 13, 14]. Then, the dispersion of noble metal nanoparticles on this support, may represent advantages for multiple potential applications, mainly in those where the electronic interactions of metallic active sites with the reducible supports, e.g. an SMSI, is required. In fact, Pt, Ru, Rh, Au, Ag and Pd have been distributed on the surface of titania nanotubes showing considerable improvements on their catalytic and photocatalytic performance [15, 16].

In this work, very uniform Ir metal nanoparticles were deposited on the surface of anatase TiO_2 particles and nanotubes. Given the predominance of (1 1 0) surface on anatase in comparison with (0 0 1) ones in TiO_2 nanotubes, different types of MSIs on Ir particles are expected to occur which could be linked to the ability of the support to decompose the Ir precursor complex allowing the complete reduction of Iridium atoms to Ir^0. The purpose of this study is to shed light on the possible MSI effect of these morphologically different supports and the reducibility of Ir nanoparticles. As a comparison to TiO_2 catalysts, Ir/alumina was used as a reference. The catalysts were evaluated in cyclohexene (CHE) hydrogenation; being a structure insensitive reaction, which allows knowing the number of Ir^0 surface atoms.

2 Experimental

2.1 Catalysts Preparation

Anatase Hombifine N, supplied by Sachtleben Chemie GmbH, was used as raw material for anatase nanoparticles support, and as a precursor throughout this study, to obtain titanate nanobubes. The specific surface area (SSA) of precursor was 347 $m^2\ g^{-1}$, and it was 100 % anatase, with a crystallite size below 8.0 nm as determined by XRD Rietveld Refinement analysis. Titania nanotubular support was synthesized by an alkali hydrothermal treatment as described elsewhere [14]. A Pural B alumina, by Sasol of 328 $m^2\ g^{-1}$ was used as inert support reference.

The three supports were impregnated as follows: 10 g of the dried support were placed in contact with 100 mL of an H_2IrCl_6 (1 wt% Ir)/ethanol (EtOH) solution. The suspension was stirred at room temperature for 2 h and heated at 343 K in a vacuum evaporator to remove excess EtOH, then, the sample was dried at 373 K in a vacuum oven overnight. The samples were calcined at 673 K under air flow in a tubular oven for 4 h. The samples were labeled: Ir/TiO_2-NP, Ir/TiO_2-NT, and Ir/Al_2O_3 for Ir deposited on anatase nanoparticles, nanotubes and alumina respectively.

2.2 Characterization

All textural properties were determined in an ASAP-2000 analyzer from Micromeritics. Specific surface area (SSA) was calculated from Brunauer–Emmet–Teller (BET) equation using N_2 physisorption at 77 K on samples previously outgassed at 623 K. Transmission electron microscopy (TEM) and scanning transmission electron microscopy (STEM), were performed both in a JEM-2200FS microscope with an accelerating voltage of 200 kV. The microscope is equipped with a Schottky-type field emission gun, and an ultra high resolution configuration (Cs = 0.5 mm; Cc = 1.1 mm; point-to-point resolution = 0.19 nm) and in-column omega-type energy filter. High angle annular dark field (HAADF) images were obtained using the HAADF detector in the STEM mode as previously reported [17].

Temperature-programmed reduction (H_2-TPR) and Temperature programmed desorption (TPD) of chemisorbed hydrogen of the catalysts was performed on an ICID apparatus model SRyC-2. The experiments were carried out using 0.1 g of oxidized catalyst. First, the sample was in situ calcined at 673 K for 1 h with a 10 K min^{-1} heating

rate and 20 mL min^{-1} air flow. Then, the sample was cooled to room temperature and a 30 % H_2/70 % N_2 purified mixed flow was fed. The H_2-TPR profiles were recorded heating at 10 K min^{-1} up to 673 K with a 20 mL min^{-1} flow rate. The hydrogen consumption as a function of reduction temperature was continuously monitored with a thermal conductivity detector (TCD). On TPD experiments, purge with N_2 (99.998 %) flow began at said temperature for 1 h, before cooling to room temperature (298 K) to start the analysis. The H_2-TPD starts by heating from room temperature to 673 K while maintaining N_2 flow of 20 mL min^{-1} and with a heating rate of 10 K min^{-1}. An Ir/H stoichiometry of 1 was assumed to calculate Ir dispersion.

Cyclohexene hydrogenation in liquid phase was chosen as a test reaction. Before the reaction, the catalysts were reduced at 673 K for 2 h on a H_2 flow. Catalytic activities were measured from 273 to 303 K, in a 100 mL batch reactor equipped with a magnetic stirrer and a reflux condenser. 4.2 mL of CHE was added to 50 mL of *n*-heptane and H_2 flow was bubbled into the liquid. In each run, 0.2 g of reduced catalyst (80–100 mesh) was loaded into the reactor. An aliquot of reaction was taken each 10 min and analyzed in a Varian CP-3600 gas chromatograph equipped with an HP-5 capillary column and Flame Ionization Detector.

Reaction rates were calculated assuming a zero kinetic reaction order: $-r_A = k$. The turn over frequency (TOF), i.e. number of cyclohexene molecules transformed into products per exposed Ir atoms per second, was calculated by expressing the reaction rate per mole of Ir exposed on the surface, as determined by TPD experiments. Turnover rate (TOR) is cyclohexene molecules transformed into products per total amount of Ir atoms per second. The apparent activation energy, *Ea*, was determined from kinetic constant data collected between 273 and 303 K. The linear form of the Arrhenius equation, $K = A \times e^{-\frac{Ea}{R \times T}}$ was used to estimate the *Ea*.

3 Results and Discussion

Textural properties of the three catalysts are shown in Table 1. The SSA of the catalysts prepared on a nanotubular support, TiO_2-NT, was very similar to that prepared on the alumina support and larger than that on anatase nanoparticles, TiO_2-NP. However, the pore volume and mean pore diameter were almost as twice as those of the catalyst prepared on Al_2O_3 support. As a comparison, most of studies, report the catalytic activity of Ir nanoparticles loaded on a reducible support having very low SSA, <100 m^2 g^{-1}, and they are compared with the activity of those deposited on an inert support Al_2O_3 or SiO_2, with SSA higher than 200 m^2 g^{-1} [18, 19]. In this case, both Ir/TiO_2-NT and Ir/Al_2O_3 showed quite similar SSA between them, hence, the accessibly of reactants to the active sites in both supports can be considered similar.

3.1 Reaction Test

The catalytic activity was measured on CHE hydrogenation reaction, which has been widely used as a model reaction for fundamental studies in the catalytic activation of C=C bonds over metallic sites [20]. Reaction rate per total Ir atoms loaded on each catalyst is shown in Table 2. Ir deposited on TiO_2-NT support hydrogenates CHE at temperatures as low as 273 K, with a turnover rate, TOR, of 2.86 mol CHE mole $Ir^{-1}s^{-1}$ whereas on Ir/TiO_2-NP and on Ir/Al_2O_3 the reaction proceeded with a TOR of 1.4 and 3.52 mol CHE mole $Ir^{-1}s^{-1}$, respectively. These differences are mainly due to the different metal dispersion on the support as can be noted in Table 2. Then, the TOF at 273 K (see Table 2) of Ir/TiO_2-NP and Ir/Al_2O_3 catalysts showed a TOF of 3.2 and 3.7 s^{-1} respectively, very close to that of Ir/TiO_2-NT, that is a TOF of 4.7 s^{-1}. Accordingly, a TOF of 4.3 s^{-1} has been reported for metallic Pt aggregates deposited on alumina [21, 22] in the liquid phase CHE hydrogenation. Nearly the same TOF was obtained for Ir nanoparticles, regardless of the dispersion values, on the nanoparticle size and on the support; which confirmed the Korous-Nowak criterion [21–23]. However, when increasing the reaction temperature, the response of these catalysts varied. An apparent activation Energy, $Ea = 56.4$ kJ mol^{-1} was obtained for Ir/TiO_2-NT, whereas $Ea = 43.2$ kJ mol^{-1} was obtained for both Ir/TiO_2 and Ir/Al_2O_3 samples, (see Table 2 and Fig. 1). Hence, these different *Ea* values suggest that Ir particles of different nature might be associated to varying reduction degrees of Ir nanoparticles.

3.2 Temperature Programmed Reduction (TPR)

The TPR profile of Ir/TiO_2-NT after annealing in air at 673 K showed a very sharp hydrogen consumption peak at

Table 1 Textural properties of Ir catalysts annealed at 673 K

Catalyst	SSA (m^2 g^{-1})	Total pore volume (cm^3 g^{-1})	Mean pore diameter (nm)
Ir/TiO_2-NT	221	0.74	9.8
Ir/TiO_2-NP	150	0.30	7.0
Ir/Al_2O_3	235	0.43	4.9

Table 2 Metal dispersion and cyclohexene hydrogenation reaction rates and TOF at 273 K

Catalyst	Ir disp (%)	TOR (mol) CHE mole Ir^{-1} s^{-1}	TOF (s^{-1})	Ea (kJ mol^{-1})
Ir/TiO_2-NT	60	2.86	4.7	56.4
Ir/TiO_2-NP	36	1.14	3.2	43.2
Ir/Al_2O_3	96	3.52	3.7	43.3

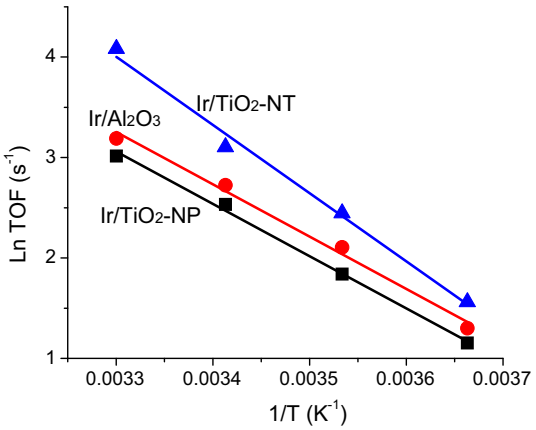

Fig. 1 Arrhenius plot for different Ir nanoparticles loaded on indicated support

390 K, corresponding to a very uniform dispersion of IrO_2 species on TiO_2-NT [24], as shown in Fig. 2. Additionally, the very low intensity peak around 489 K has been attributed to agglomerated IrO_2 crystallites [25, 26]. Finally, two H_2 consumption peaks at 623 and 693 K, corresponded to surface and bulk reduction of the TiO_2 support, as reported elsewhere [27].

In the TPR profile of Ir/TiO_2-NP catalyst, a very low intensity peak at 390 K was observed and, similar to the above catalyst, it comes from IrO_2 species [24] in stronger interaction with TiO_2-NP support (compared with those supported on TiO_2-NT in Fig. 2). Around 489 K, a H_2 consumption peak was observed, suggesting the presence of some agglomerated IrO_2 crystallites [25, 26]. This

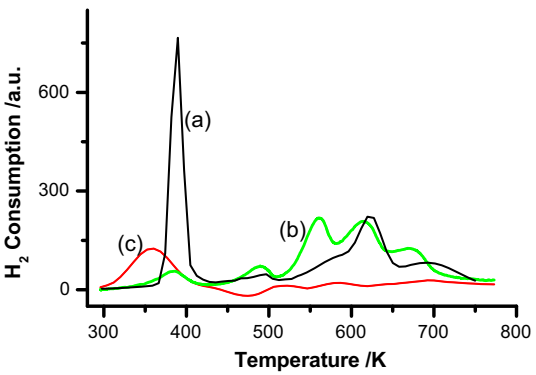

Fig. 2 Temperature programmed reduction of: *a* Ir/TiO_2-NT, *b* Ir/TiO_2-NP and *c* Ir/Al_2O_3

consumption peak was a little bit more intense than that observed on TiO_2-NT support. Around 561 K, a very well defined H_2 consumption peak was observed in Ir/TiO_2-NP, whereas in Ir/TiO_2-NT sample, a shoulder at this temperature suggest the presence of a lower number of these reducible species. Therefore, this peak may correspond to the reduction of the $Ir^{\delta+}$ acting as anchoring sites at the interface of the metal nanoparticle with the support [28]. The last two peaks at 615 and 673 K in the TPR profile of Ir/TiO_2-NP, correspond mainly to surface and bulk reduction of TiO_2 support [27].

The TPR profile of Ir/Al_2O_3 catalyst (Fig. 2) showed hydrogen consumption centered a 358 K followed by hydrogen desorption, which is characteristic of uniformly dispersed iridium oxide on alumina systems [24]. The fact that the reduction temperature was around 358 K, somewhat lower than those observed when Ir was dispersed in nanotubular and nanoparticles TiO_2 anatase, suggests the presence of IrO_2 species with smaller size in higher interaction with Al_2O_3 support than those on TiO_2 supports. After this H_2 desorption process, another H_2 consumption peak appeared at 517 K, characteristic of the reduction of larger IrO_2 agglomerates [25, 26]. The two less intense and broad peaks with maximum at 583 and 693 K, are likely associated to the gradual reduction of the $Ir^{\delta+}$ ions remaining in the interface of the two types of Ir particles on the Al_2O_3 support.

It is known that some noble metal cations are responsible of the higher dispersion of Pt in Pt/Al_2O_3, acting as anchoring sites and making the Pt nanoparticles more stable against sintering [28]. The interaction between these noble metal cations have been calculated to be stronger on Al^{3+}, and O^{2-} ions rather than on OH^- anions [29]. This fact suggests that the creation of vacancies on the support surface will increase the metal support bonding because metal cations on the support surface are in direct contact with noble metal atoms. Recently, we have reported that distinct surface physicochemical properties of TiO_2 depend on the morphology of titania anatase [30], i.e. nanotubes and nanofibers of TiO_2 do not expose coordinatively unsaturated sites (CUS) Ti^{4+} or basic O^{2-} sites, which typically occur on TiO_2 anatase nanoparticles. These differences on the surface properties might be responsible for different interactions of IrO_2 nanoparticles on TiO_2 having different morphology. On TiO_2 nanotubes, there are not CUS sites, they expose only OH^- anions on the surface,

therefore, the interaction between the IrO_2 nanoparticles with TiO_2 nanotubes surface is weaker through OH^- anions, whereas it is stronger when it operates on TiO_2 nanoparticles through Ti^{4+} CUS sites exposed on the surface [30]. Therefore, the higher intensity of the H_2 consumption peak at 390 K in the TPR profile of Ir/TiO_2-NT sample is precisely due to this weaker interaction of IrO_2 on TiO_2-NT surface, which allows the complete reduction of the whole IrO_2 nanoparticle at this low temperature. In contrast, on Ir/TiO_2-NP the intensity of the H_2 consumption peak at 390 K was very low, suggesting incomplete reduction of the IrO_2 nanoparticles, due to a stronger interaction with anatase TiO_2-NP and the clear H_2 consumption peak at 561 K, confirming the reduction of $Ir^{\delta+}$ cations acting as anchoring sites of the metal support interface. Nonetheless, a shoulder at ~561 K in the TPR profile of Ir/TiO_2-NT catalyst do not allow us to discard the reduction of a small amount of $Ir^{\delta+}$ cations in the interface of Ir nanoparticles, which may be responsible to keep the high dispersion and to stabilize Ir nanoparticles against sintering [28].

In the case of alumina support, H_2 consumption of IrO_2 occurred at lower temperature than that on TiO_2-NP and TiO_2-NT, pointing out the reduction of smaller IrO_2 species. Here, the fact that the intensity of the reduction peak was lower than that observed on Ir/TiO_2-NT catalyst suggests a stronger interaction of IrO_2 nanoparticles with the CUS sites of Al^{3+} inhibiting the complete reduction of the Ir cations. Two broad H_2 consumption peaks around 573 and 693 K confirm that the reduction of the $Ir^{\delta+}$ cations, on the interface of Ir nanoparticles with the alumina surface, occurs gradually as the reduction temperature increased.

3.3 Temperature-Programmed Desorption of Chemisorbed H_2

H_2 desorption profiles from the three catalysts was made up of four peaks, corresponding to different metal-hydrogen interactions (see Fig. 3). In general, the peaks below 450 K, are usually assigned to hydrogen chemisorbed on the metallic Ir aggregates, whereas the higher temperature peaks have been assigned to hydrogen strongly chemisorbed on extremely small Ir clusters [31]. In fact, in tetrairidium clusters deposited on MgO, a large amount of H_2 is preferentially chemisorbed at 673-713 K and no peaks below 450 K were detected [32], indicating that the H_2 desorption peak at about 673 K is associated indeed to very small Ir clusters. Thus, in our TPD results, the Ir/Al_2O_3 catalyst chemisorbs H_2 with high intensity in both: (i) the low temperature peak (358 K), from H_2 chemisorbed on metallic Ir nanoparticles and, (ii) the high temperature peak (673 K) associated to H_2 in strong interaction with very small Ir clusters dispersed on Al_2O_3. On the other hand, on Ir/TiO_2-NP, less intense H_2 desorption peaks were observed, two peaks were distinguished at 323 and 388 K, from H_2 interaction on two different metallic Ir sites [24]; the other high temperature H_2 desorption peaks at 488, 580 and 673 K correspond to H_2 strongly bounded to Ir nanoparticles having strong interaction with the support. Ir/TiO_2-NT had a more intense H_2 desorption peak at 390 K, and a very small H_2 desorption peak appeared at 620–673 K, suggesting that in this catalyst, H_2 is mainly chemisorbed on Ir metallic sites, confirming the metallic character of Ir nanoparticles deposited on TiO_2-NT. Since H_2 desorption peaks at ca. 488 and 580 K remain nearly constant in all samples, it appears that H_2 desorption peak at 673 K is directly related to the metal support interaction, such as in Al_2O_3 and TiO_2-NP. Accordingly, the support acts as a ligand shell to Ir particles affecting their metallic character, *i.e.* Ir nanoparticles are not completely metallic and H_2 is bonded strongly on these Ir particles inhibiting their catalytic activity [32, 33], as shown in Fig. 1.

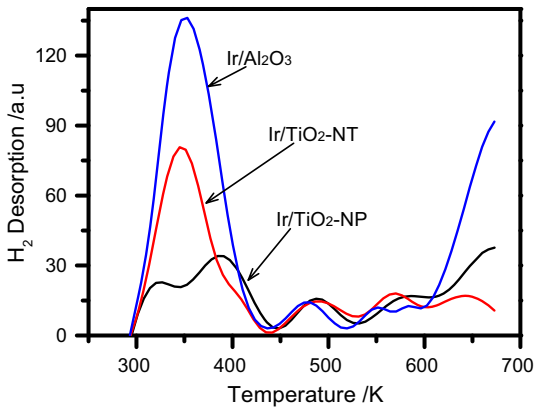

Fig. 3 Temperature programmed desorption profile for hydrogen desorption from Ir nanoparticles loaded on indicated support

Ir dispersion reported in Table 2 was calculated taking into account the total amount of H_2 chemisorbed on each sample. An Ir/H stoichiometry of 1.0 was used to estimate Ir dispersion used for TOF calculation, also reported in Table 2.

3.4 Electron Microscopy of Supported Ir Nanoparticles

Dispersion and particle size of Ir nanoparticles onto the different supports were directly observed and measured by STEM (see Fig. 4). Here, the images show small bright dots from particles made up of Ir atoms aggregates dispersed on the supports. Nanoparticles avg. size on each sample was done by statistically measuring 150 dots. The Ir particles dispersed on TiO_2-NP, on TiO_2-NT and on alumina (Fig. 4a, c, e, respectively) had avg. size around 1.3,

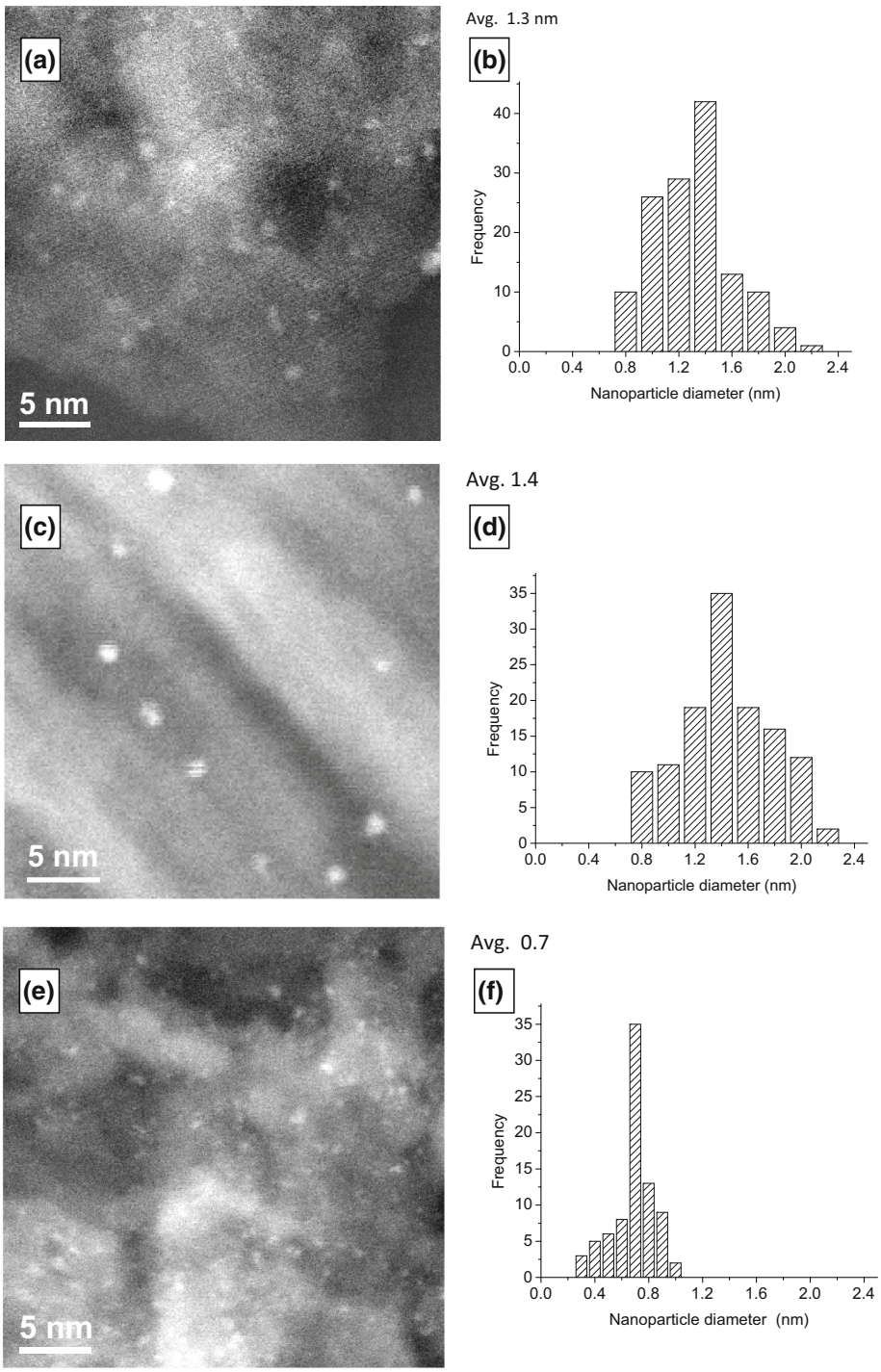

Fig. 4 HAADF images of metallic Ir nanoparticles impregnated on: **a** anatase nanoparticles, **c** anatase nanotubes, **e** alumina; and **b**, **d** and **f**, their corresponding particle size distribution plots

1.4 and 0.7 nm with a standard deviation of 0.12, 0.11, and 0.07 nm, respectively. The dispersion range remained between 0.8 and 2.2 nm, on titania supports as indicated in the size distribution plots in Fig. 4b, d and between 0.3 and 1.0 nm for alumina, as in Fig. 4f. The chemical nature of the support strongly affects the interaction with Ir particles, i.e. the stronger the metal support interaction, the lower the metal particle size; therefore, the interaction of Ir particles with alumina is stronger than that on TiO_2. However, though Ir particles on TiO_2-NP and TiO_2-NT have practically the same sizes, a different interaction way is expected on TiO_2-NP and on TiO_2-NT, as suggested on the above TPR and TPD results. In fact, by analyzing the contrast of the metal particles dispersed on TiO_2-NP and on TiO_2-NT supports, in HAADF images (Fig. 4a, c), it can be observed that the particles on nanotubes are brighter than those on

anatase particles when comparing two particles with the same diameter. This difference originates on their atomic density, suggesting different types of interactions between the Ir nanoparticles and the surfaces of the TiO_2-NP and TiO_2-NT nanoparticles. These results prompted a more detailed HRTEM study.

Ir nanoparticles on TiO_2-NP and TiO_2-NT images are shown in Fig. 5, where the interplanar distances correspond to the {111} and {002} planes of the fcc metal Ir phase viewed along the [110] direction. Additionally, (220) planes of anatase phase were observed in the HRTEM image of the Ir/TiO_2-NP sample, (see Fig. 5a). The image of the nanoparticle is a bidimensional projection of six surface planes; four correspond to the {111} and two to the {002} faces. The 111° and 126° internal angles between the sides of the hexagon, the surface planes and the hexagonal shape in the projection direction of the cubic structure, suggest that the nanoparticle has a cuboctahedral morphology with eight {111} surfaces truncated with six {002} surfaces, once in their 3D projection. Ir particles, deposited on TiO_2-NT, must have the same morphology; however, the contrast of these particles (Fig. 5b) is quite different from those on TiO_2-NP (Fig. 5a). Since these varying contrast levels are likely caused by different atomic density or different stacking layers of Ir atoms in the nanoparticles, two growth models of Ir nanoparticles were proposed by matching the best coupling of Ir on the interface of the titanias, (see in Figs. 6a, 7a).

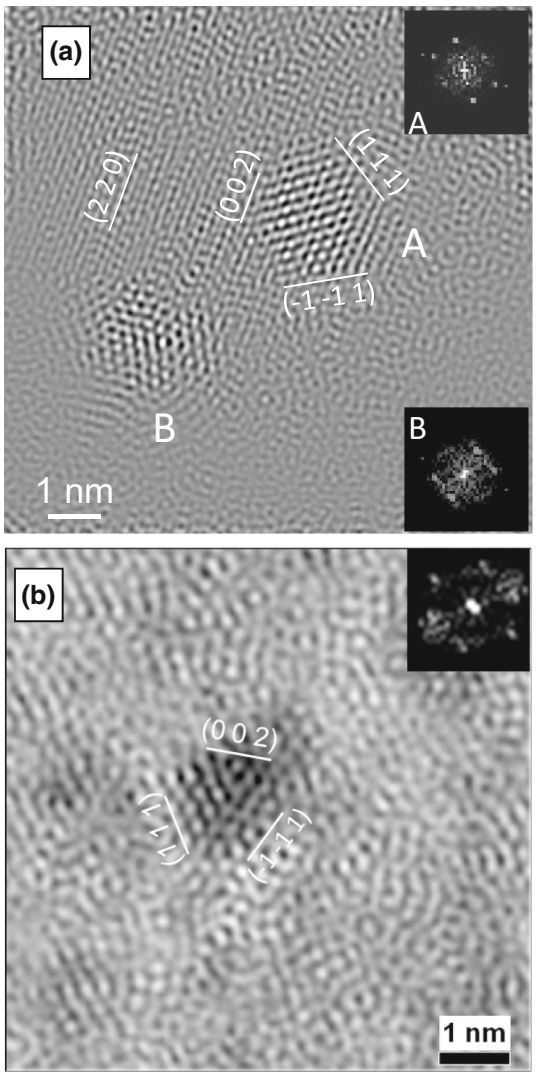

Fig. 5 HRTEM image of metallic Ir nanoparticles on: **a** anatase nanoparticles and **b** anatase nanotubes

On TiO_2-NP (see Fig. 6a) the flat surface of anatase particles allows the interaction and growth on the contact surface of Ir atoms, generating a half truncated cuboctahedral particle. In contrast, on TiO_2-NT, the curved surface of the nanotube limit the interaction and contact surface with Ir atoms favoring a full growth of a complete cuboctahedral nanoparticle (see Fig. 7a). Since HAADF and HRTEM images of the particles are 2D projections, the size and the hexagonal shape generated by both half truncated and full cuboctahedral nanoparticles are nearly the same. Then, theoretical calculations of both nanoparticles models of HRTEM images were carried out.

3.5 Modeling Supported Ir Particles

The fcc structure atomic models of Ir, space group *Fm3m* (225); and the tetragonal structure of anatase TiO_2, space group *I41/amd* (141) were used in this study. The Ir particle-model was built considering a cuboctahedral morphology with a magic number of 147 atoms in three layers [34]. The model size is ~1.3 nm [35], being the most stable atomic distribution with the lowest internal energy and 2D projection along the <110> direction, generating a hexagonal shape. This Ir model was stacked on the surface of nanoparticle models of anatase and nanotubes TiO_2. In the case of TiO_2-NP, the (110) surface plane was selected, considering that (220) planes were observed in the HRTEM image; while the TiO_2-NT exposes the (001) surface. According to HAADF-STEM and HRTEM results, the Ir particles deposited on TiO_2-NP are likely to have lower atomic density than those on TiO_2-NT. Brighter Ir nanoparticles on TiO_2-NT in HAADF-STEM image and darker in HRTEM image are displayed. In other words, a half particle of three Ir layers (92 atoms) was stacked on the (110) surface; and a full particle (147 atoms) was stacked on the nanotube surface. These particles produce, in the 2D projection, a hexagonal geometric shape when oriented along to the [110] direction. Bonds between the metal phase and the supports were assumed to be made up of single metal–metal coordination and fourfold metal–oxygen coordination at the metal support interface, as

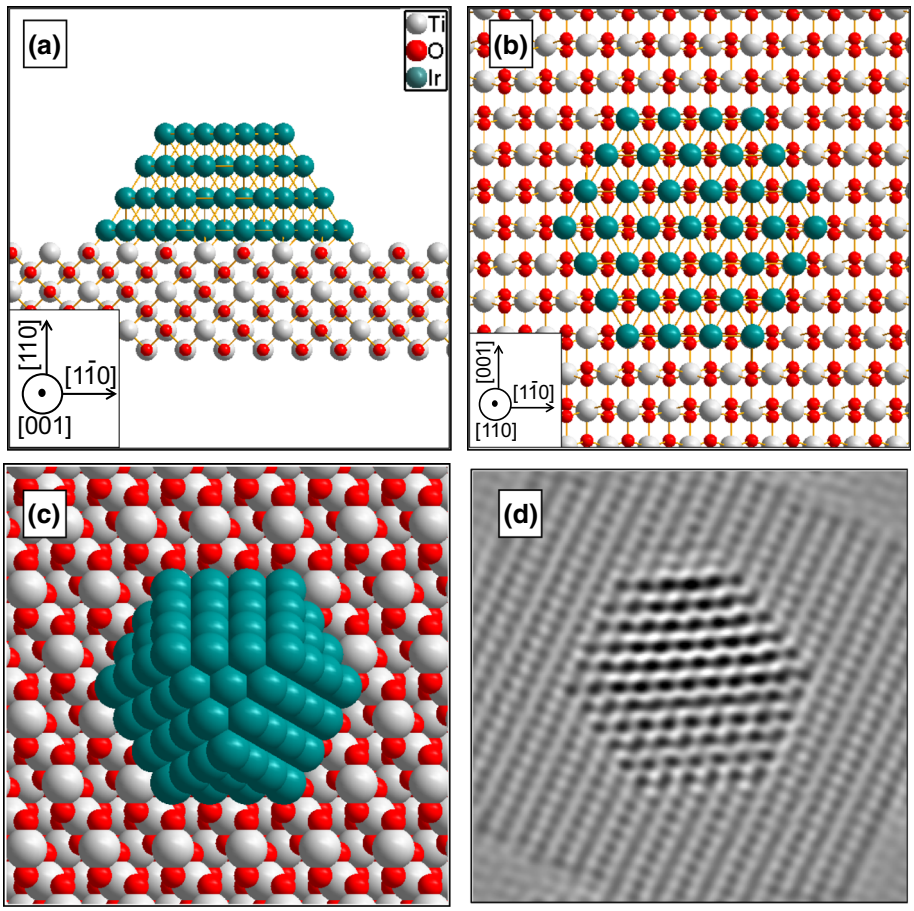

Fig. 6 **a** Atomic model showing the half of a cuboctahedral Ir nanoparticle stacked on the (110) anatase surface. The model is projected along [001] direction of the TiO_2 (*side view*). **b** Model projected along the [1 1 0] direction of the TiO_2 (*top view*), **c** Tridimensional projection of the Ir nanoparticle on the (110) surface of the anatase particle (*top view*) and **d** simulated HRTEM image of the Ir nanoparticle oriented along the [110] direction

reported elsewhere [36, 37]. The interface planes on both structures were aligned in order to approximate the Ir atoms as close as possible to the Ti atoms. The (110) TiO_2 surface plane observed along the [001] TiO_2 direction is shown in Fig. 6a. Here, a direct interaction between Ti and Ir atoms can be done by an epitaxial growth of the (220) Ir||(2-20) TiO_2. The d-spacings between these planes are very close, 0.133 and 0.135 nm, respectively, inducing a very small 1.5 % lattice distortion on the surface atoms. The first layer of Ir atoms on the metal-support interface of the (110) TiO_2 surface is shown on Fig. 6b, here, the distance between rows of Ir atoms is 0.235 nm and matches very well with the d-spacing of the (1-1 2), (1-1-2) and (004) TiO_2 planes, being 0.233, 0.233 and 0.237 nm, respectively. Ir atoms atop the Ti atoms on the (110) TiO_2 surface can be appreciated in Fig. 6b.

A 3D projection of the Ir particle deposited on (110) surface of the anatase TiO_2 particle is depicted in Fig. 6c. Only seven surface faces are appreciated, four {111} faces and three {100} faces. This model was subsequently oriented along to the [110] Ir direction, to obtain the calculated HRTEM image, (see Fig. 6d). The theoretical calculation was performed by the multislice technique [38]. In the simulated HRTEM image, an intensity pattern of bright dots, quite similar to the intensity pattern of experimental atomic resolution image in Fig. 5a was observed. This result confirms that Ir particles deposited on the (110) surface of anatase have half-truncated cuboctahedral morphology.

In the case of TiO_2-NT, anatase phase exposes mainly the (001) surface [14, 39]. On this surface, the closest approximation between Ir and Ti atoms were obtained when the (111) Ir plane atoms are aligned with (110) planes of TiO_2-NT (see Fig. 7a). The d-spacing of the (110) planes of TiO_2-NT is 0.267 versus 0.235 nm of Ir rows, giving a lattice mismatch of 13.6 % which is higher than that of Ir on (110) anatase surface in TiO_2-NP. On the metal support interface only one row of Ir atoms can be located atop the Ti atoms of the (110) plane, the other Ir rows remain away from the top of Ti atoms in this plane, and metal–metal coordination is not possible. In other words, if SMSI proceeds by the metal–metal coordination of the interface [37], on the (001) surface of TiO_2-NT, this type of interaction can take place only on a single row of Ir atoms, generally on the edge of the nanoparticle, that is, on the {110} planes (see Fig. 7a, b). In contrast, on the (110)

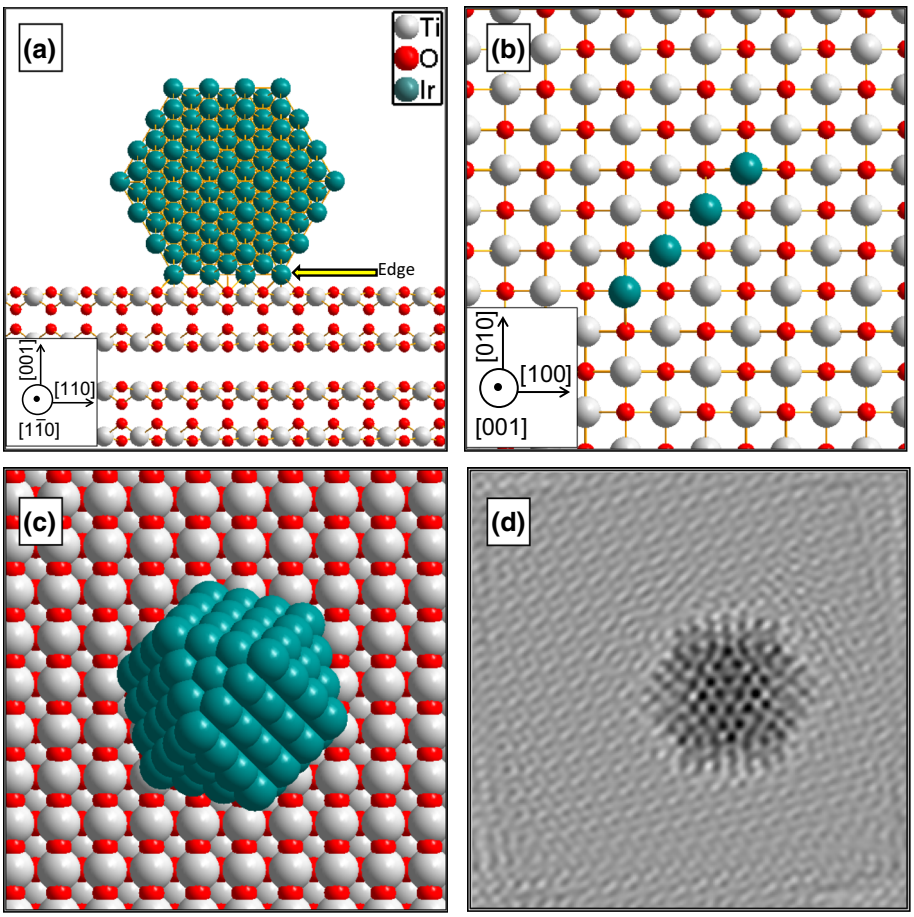

Fig. 7 **a** Atomic model showing the full particle stacked atop of the Ti atoms located in the (1-10) plane of the anatase nanotube. The model is projected along to the [1 -1 0] direction of the TiO_2-NT(*side view*), **b** View of model along to [001] direction of the TiO_2-NT (*top view*) showing an edge of the full Ir cuboctahedral particle stacked on the Ti atoms corresponding to (1 -1 0) plane, **c** Tridimensional projection of the Ir nanoparticle on the (001) surface of the anatase nanotube (*top view*) and **d** simulated HRTEM image of the Ir nanoparticle oriented along to the [110] direction

surface of TiO_2-NP support, all the rows of Ir atoms are atop the Ti atoms, and metal–metal coordination occurs on all Ir and Ti atoms of the metal support interface as well, suggesting a stronger metal support interaction. A 3D view of the model, where the metallic particle is stacked on one of their edges with Ti atoms via the (110) plane, is shown in Fig. 7c. As can be noted, the three dimensional projection of Ir/TiO_2-NT shows exactly the same surfaces than those observed in the Ir atomic model stacked on the (110) surface of TiO_2-NP (see Fig. 6) with only half of the nanoparticle. However, the simulated HRTEM images of both models differs, a hexagonal dark contrast image was obtained for the complete cuboctahedral particle on the (001) surface of TiO_2-NT, such as the experimental atomic resolution image obtained for this sample in Fig. 5b. These differences were also observed clearly in the brightness intensity of the metallic nanoparticles in the HAADF images, (see intensity profile in Fig. 8). In both samples, Ir nanoparticles had similar diameter but different intensity. The Ir nanoparticles deposited on TiO_2-NT are more intense than those deposited on TiO_2-NP. Theoretically, the brightness intensity increases with increasing the atomic number or the number of atoms in the nanoparticle. Since the atomic number is constant, the variation of intensity profile must correspond to metallic nanoparticles with different atomic density. In fact, theoretical calculations of brightness intensity obtained from models in Figs. 6a and 7a; match very well with the experimental intensity profile, which confirm that the difference in intensity was produced by the number of atoms present in the nanoparticles.

From these results, it can be concluded that Ir nanoparticles interact stronger with the (110) surface of anatase nanoparticles, TiO_2-NP, than with the (001) surface of TiO_2-NT. This strong interaction can be reasonably explained by the perfect lattice matching between Ir and Ti atoms at the metal-support interface on the (110) surface of anatase nanoparticles, which means that all Ir atoms are able to form metal–metal bonds with Ti atoms of the support. On the other hand, at (001) surface of anatase nanotubes, only a row of Ir atoms can be located atop the Ti atoms to form metal–metal bond, then the interaction can be done by a row of Ir atom on the edge of the particle and it is not as strong as that on TiO_2-NP. The different metal-support interactions originated by different surface planes exhibited by anatase change the Ir nanoparticle morphology from complete cuboctahedral for TiO_2-NT to

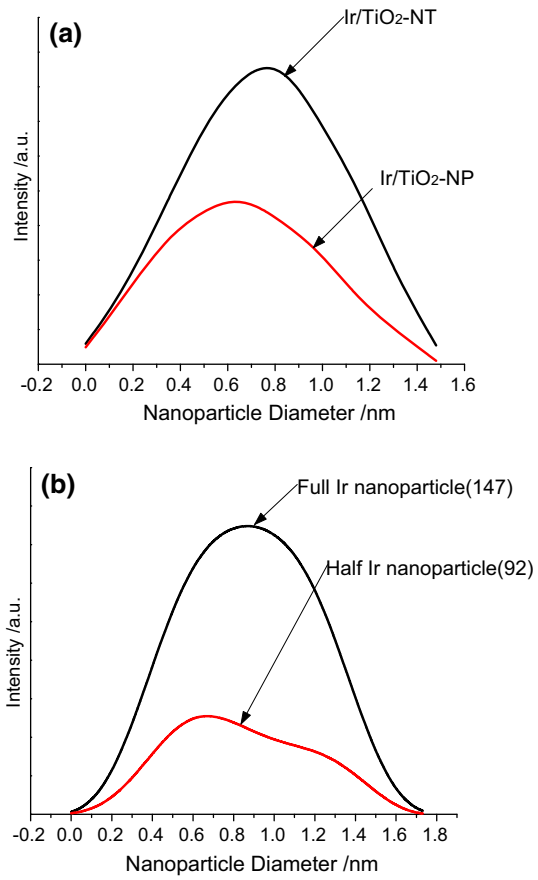

Fig. 8 **a** Experimental intensity profile obtained from HAADF images of single Ir nanoparticles deposited on anatase nanoparticles and nanotubes and, **b** theoretical intensity profile calculated from atomic models proposed for the Ir nanoparticles of 92 and 147 atoms, respectively. The atomic models of the nanoparticles were oriented along to the [111] direction

half truncated cuboctahedral for TiO_2-NP. Therefore, in the half cuboctahedral particles deposited on TiO_2-NP, a large number of Ir atoms remain partially reduced at the metal-support interface bonded as a single Ir–Ti bond and four Ir–O bonds [37], whereas in complete cuboctahedral particles deposited on TiO_2 nanotubes, only a few Ir atoms remain partially reduced at metal support interface. This fact, explain the very different TPR profile, shown in Fig. 2. Most of Ir atoms deposited on TiO_2-NT reduce at 390 K with a very intense H_2 consumption peak. In contrast, Ir atoms deposited on TiO_2-NP are characterized by a very low H_2 consumption peak at 390 K, being preferentially reduced at 561 K corresponding to the reduction of larger amount of Ir atoms located at the metal-support interface.

3.6 Supported Ir Nanoparticle Morphology and Catalytic Activity

Supported noble metal particles at nanoscale clusters preferentially adopt the most stable shape and morphology, which is the hemispherical cuboctahedra cluster shapes [40] such as those observed on (110) surface of anatase, Ir/TiO_2-NP. However, recently Koningsberger et al. [41, 42] demonstrated that more spherical Pt nanoparticles were obtained by changing the ionicity of the surface O atoms adding an alkaline modifier to the alumina support, whereas in a less electron rich surface, that is, an acidic alumina support, half spherical Pt nanoparticles were deposited. In this work, we have demonstrated that the shape and morphology of supported metallic nanoparticles depend not only on the ionicity of the support surface but also on the lattice match in metal support interface between the fcc cubic structure of the metal nanoparticle and the support exposed surface.

Hence, the (110) surface of anatase, match very well with the (111) face of fcc structure of Ir nanoparticles, locating Ir atoms atop the Ti atoms and SMSI takes place among them, yielding half cuboctahedra shaped nanoparticles. On the (001) surface exhibited by nanotubes, only a row of Ir atoms are localized atop the Ti atoms, probably one edge row of Ir atoms acts as a metal support interface allowing the complete grow of the cuboctahedra.

Ir nanoparticles deposited on Al_2O_3 support remained at subnanometer scale, <1.0 nm, atomic resolution observation by HRTEM was impossible, then, it was not modelled. However, SMSI can be inferred and particles are expected to be nearly half-spherical, due to the low number of Ir atoms in this cluster, <10 atoms; however, it is not possible to define the shape of this nanoparticles.

CHE hydrogenation has been a thoroughly investigated as structure-insensitive reaction, in metal particles exhibiting different surface planes, in a broad crystallite size and dispersion range; the reaction proceeding at approximately the same turnover frequency [22, 23, 43–45]. In this work, the kinetic data presented in Fig. 1 and Table 2 showed that both Ir nanoparticles deposited on TiO_2-NP and Al_2O_3, with nearly the same metal content ($\sim$1.0 wt%) and same crystallite habit (e.g. half truncated cuboctahedral morphology), showed quite similar TOF (3.2 s^{-1}) at 273 K in CHE hydrogenation reaction; and when Ir^0 particles are deposited on TiO_2-NT, where complete cuboctahedral particle grew, the TOF value at 273 K was slightly higher (4.7 s^{-1}). In fact, the Arrhenius plot of Fig. 1, that is, the activation energy, *Ea*, was different in both kind of Ir^0 particles. Complete cuboctahedral particles activate more largely with temperature than half truncated cuboctahedral ones, see Table 2.

This later fact point out the different nature of metal particles due to an effect of the metal support interface acting as a ligand affecting the metallic character or electronic properties of the Ir atoms in the nanoparticles, rather than an effect of nanoparticle size [46]. Accordingly, Pt particles loaded on a basic support with electron-poor

surface oxygen atoms, show a more spherical Pt particles shape [41, 42], and metallic character for sizes as small as 1.2 nm. In contrast, in Pt particles on acidic supports with electron- rich surface oxygen atoms, having half spherical Pt particles shapes [41], Pt particles did not show metallic behavior until size was larger than 2.0 nm [47]. In other words, the complete cuboctahedral Ir particles loaded on TiO_2-NT of $\sim$1.4 nm have a total metallic character, while those with half truncated cuboctahedral morphology deposited on TiO_2-NP, with the same size, are metallic screened due to the SMSI and do not show metallic behavior when having $\sim$1.4 nm. These differences in metallic character reasonably explain the very different catalytic performance of Ir nanoparticles on CHE hydrogenation. From these results, it can be remarked that CHE hydrogenation reaction is a structure insensitive reaction as long as the particles have well defined metallic character with same morphology, but it is strongly sensitive to the metallic screening from the ligand shell provided by the SMSI [32, 46], inhibiting the complete reduction of Ir particles. The limit of particle size where Ir particles manifest metallic character varied as a function of the metal support interaction which in turn controls the morphology of Ir nanoparticles. Indeed, for weaker metal-support interaction, such as in Ir/TiO_2-NT, complete cuboctahedral particles of 1.4 nm size are formed, showing a metallic behavior which favor the hydrogenation of CHE with a TOF of 4.7 s^{-1} at 273 K, nearly comparable to TOF of 4.3 s^{-1} reported for metallic Pt aggregates deposited on alumina [32, 33].

Finally and as a comparison, in Ir/Al_2O_3, where the strongest metal support interaction occurs, we infer that half cuboctahedral or semispherical particles of 0.7 nm mean size are present, and they must be made up of less than 10 Ir atoms, the metallic screening being as on Ir/TiO_2-NP sample. Thus, these particles are practically as active as Ir/TiO_2-NP in CHE hydrogenation, showing a TOF of 3.7 s^{-1}.

4 Conclusions

When aiming at well dispersed nanometric Ir particles as supported catalysts for a given hydrogenation reaction, the following findings should be taken into account. A reducible support as TiO_2 is essential to have Ir nanoparticles in the correct size. However, in order to modulate MSI between Ir particles and TiO_2 support, a morphologically appropriate TiO_2 must be chosen: TiO_2 nanotubes are much better than TiO_2 nanoparticles. The morphology of TiO_2, or in more precise words, the crystal planes that eventually will interact with deposited Ir entities will strongly affect the morphology of the resulting Ir particles, producing half truncated cuboctahedral Ir nanoparticles (on TiO_2 anatase nanoparticles) or complete cuboctahedral ones (on TiO_2 anatase nanotubes). The later catalyst showed a TOF of 4.7 s^{-1} at 273 K in CHE hydrogenation, 1.5 times higher than that of Ir on TiO_2 nanoparticles of 3.2 s^{-1}. The origin of these two Ir nanoparticles shapes is caused by proper crystal planes matching between the support and the noble metal particles. For instance, planes dimensions between Ir nanoparticles and anatase is so close that a SMSI produces only half of a cuboctahedral Ir particle, withdrawing metallic character from the Ir particles. In contrast, planes alignment between TiO_2 nanotubes and Ir nanoparticles allow Ir nanoparticles to grow to a complete cuboctahedral shape, having a poor MSI, and producing Ir nanoparticles with high metallic character. These Ir nanoparticles on TiO_2 nanotubes were more active in CHE hydrogenation than their truncated Ir counterparts on anatase nanoparticles. As a comparison, Ir supported on Al_2O_3, where a remarkable SMSI generated Ir nanoparticles smaller than $\sim$0.7 nm, with a likely truncated shape, were as active as Ir/TiO_2-NP in cyclohexene hydrogenation in all the reaction temperature range studied. It is clear from this study that, nanometric Ir particle size, and high dispersions alone, are not the only factors to be considered when developing efficient hydrogenating catalysts; but, additionally, SMSI and concomitant Ir nanoparticle morphology and reducibility aspects must be taken into account to understand the differences in catalytic activity.

References

1. Siegel RW, Hu E, Roco MC (Eds.) (1999) Nanostructure science and technology, Springer (former KluwerAcademic Publishers) Dordrecht, The Netherlands. http://www.wtec.org/loyola/nano
2. Förster S, Antonietti M (1998) Adv Mater 10:195–217
3. Trindade T, Brien PO, Pickett NL (2001) Chem Mater 13:3843–3858
4. Higatsberger MJ (1981) In: Marton C (ed) Advances in electronics and electron physics, vol 56. Academic Press, New York
5. Narayanan R, El-Sayed MA (2004) J Am Chem Soc 126:7194–7195
6. Resasco DE, Haller GL (1982) Stud Surf Sci Catal 11:105–112
7. Tauster SJ, Fung SC, Baker RTK, Horsley JA (1981) Science211:1121–1125
8. Haller GL, Resasco DE (1989) Adv Catal 36:173–235
9. Resasco DE, Haller GL (1984) J Phys Chem 88:4552–4556
10. Do PT, Alvarez WE, Resasco DE (2006) J Catal 238:477–488
11. Kasuga T, Hiramatsu M, Hoson A, Sekino T, Niihara K (1998) Langmuir 14:3160–3163
12. Du GH, Chen Q, Che RC, Yuan ZY, Peng LM (2001) Appl Phys Lett 79:3702–3704
13. Cheng C, Teng H (2004) Chem Mater 16:4352–4358
14. Toledo Antonio JA, Capula S, Cortés-Jácome MA, Angeles-Chávez C, López-Salinas E, Ferrat G, Navarrete J, Escobar J (2007) J Phys Chem C 111:10799–10805
15. Yu KP, Yu WY, Kuo MC, Liou YC, Chien SH (2008) Appl Catal B 84:112–118

16. Bavykin DV, Lapkin AA, Plucinski PK, Friedrich JM, Walsh FC (2005) J Catal 235:10–17
17. Toledo-Antonio JA, Angeles-Chávez C, Cortés-Jacome MA, Cuauhtémoc-López I, López-Salinas E, Pérez-Luna M, Ferrat-Torres G (2012) Appl Catal A Gen 437:155–165
18. Rojas H, Borda G, Reyes P, Martínez JJ, Valencia J, Gacia Fierro JL (2008) Catal Today 133:699–705
19. Kluson P, Cerveny L (1995) Appl Catal A 128:33–40
20. Yang M, Rioux RM, Somorjai GA (2006) J Catal 237:255–266
21. Madon RJ, ÓConnell JP, Boudart M (1978) AIChE J 24:904–910
22. Boudart M, Sajkkowski D (1991) J Trans Faraday Soc 92:57–67
23. Gonzo EF, Boudart M (1978) J Catal 52:462–471
24. Kip BJ, Van Grondelle J, Martens JHA, Prins R (1986) Appl Catal 26:353–373
25. Huang YJ, Fung SC (1991) J Catal 131:378–384
26. Huang YJ, Fung SC, Gates WE, McVicker GB (1989) J Catal 118:192–202
27. Zhu H, Qin ZI, Shan WJ, Shen WJ, Wang JG (2004) J Catal 225:267–277
28. Huizinga T, Prins R (1983) J Phys Chem 87:2264–2267
29. Anderson AB, Ravimohan C, Mehandru SP (1987) Surf Sci 183:438–448
30. Toledo-Antonio JA, Cortés-Jacome MA, Navarrete J, Angeles-Chávez C, López-Salinas E, Rendón-Rivera A (2010) Catal Today 155:247–254
31. Miller JT, Meyers BL, Modica FS, Lane GS, Vaarkamp M, Koningsberger DC (1993) J Catal 143:395–408
32. Xu Z, Gates BC (1995) J Catal 154:335–344
33. Xu Z, Xiao FS, Purnell SK, Alexeev O, Kawi S, Deutsch SE, Gates BC (1994) Nature 372:346–348
34. Martin TP, Bergman T, Gohlich H, Lange T (1991) J Phys Chem 95:6421–6429
35. Bokhimi X, Zanella R, Angeles-Chávez C (2010) J Phys Chem 114:14101–14109
36. Mulder CAM, Klomp JTJ (1985) J Phys Colloques 46:C4-111–C4-116. doi:10.1051/jphyscol:1985412
37. Van Zon FBM, Maloney SD, Gates BC, Koningsberger DC (1993) J Am Chem Soc 115:10317–10326
38. Rodriguez AG, Beltran LM (2001) Rev Latin Am Metal Mat 21:46–50
39. Rendón-Rivera A, Toledo-Antonio JA, Cortés-Jácome MA, Angeles-Chávez C (2011) Catal Today 166:18–24
40. Frenkel AI, Hills CW, Nuzzo RG (2001) J Phys Chem B 105:12689–12703
41. Stakheev AY, Zhang Y, Ivanov AV, Baeva GN, Ramaker DE, Koningsberger DC (2007) J Phys Chem C 111:3938–3948
42. Ramaker DE, Teliska M, Zhang Y, Stakheev AY, Koningsberger DC (2003) Phys Chem Chem Phys 5:4492–4501
43. Boudart M (1969) Adv Catal 20:153–166
44. Leclercq G, Boudart M (1981) J Catal 71:127–135
45. Boudart M, McConica MC (1989) J Catal 117:33–41
46. Zhao A, Gates BC (1996) J Am Chem Soc 118:2458–2469
47. Ramaker DE, Oudenhuijzen MK, Koningsberger DC (2005) J Phys Chem B 109:5608–5617